

Metal Site-Specific Electrostatic Field Effects on a Tricopper(I) Cluster Probed by Resonant Diffraction Anomalous Fine Structure (DAFS)

Pinar Alayoglu, Tieyan Chang, M. Victoria Lorenzo Ocampo, Leslie J. Murray, Yu-Sheng Chen, and Neal P. Mankad*



Cite This: <https://doi.org/10.1021/acs.inorgchem.3c02472>



Read Online

ACCESS |

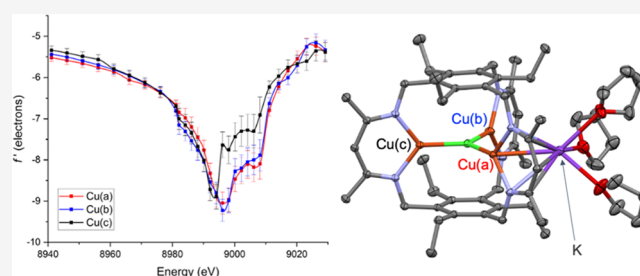
Metrics & More

Article Recommendations

Supporting Information

ABSTRACT: Studies of multinuclear metal complexes are greatly enhanced by resonant diffraction measurements, which probe X-ray absorption profiles of crystallographically independent metal sites within a cluster. In particular, X-ray diffraction anomalous fine structure (DAFS) analysis provides data that can be interpreted akin to site-specific XANES, allowing for differences in metal K-edge resonances to be deconvoluted even for different metal sites within a homometallic system. Despite the prevalence of Cu-containing clusters in biology and energy science, DAFS has yet to be used to analyze multicopper complexes of any type until now.

Here, we report an evaluation of trends using a series of strategically chosen Cu(I) and Cu(II) complexes to determine how energy dependencies of anomalous scattering factors are impacted by coordination geometry, ligand shell, cluster nuclearity, and oxidation state. This calibration data is used to analyze a formally tricopper(I) complex that was found by DAFS to be site-differentiated due to the unsymmetrical influence on different Cu sites of the electrostatic field from a proximal K^+ cation.



INTRODUCTION

Copper clusters play important roles in many settings across various length scales. For example, nanoscale copper clusters are amongst the most promising catalyst materials for both CO_2 hydrogenation and CO_2 electroreduction.^{1,2} Copper clusters in biology are responsible for several functions including electron transfer (e.g., Cu_A) and redox catalysis (e.g., Cu_Z , multicopper oxidases).³ As such, it is important to understand fundamental structure–property relationships dictating copper cluster behavior. Particularly detailed information can be gained from measurements that can resolve individual metal sites within a homometallic cluster.

One such method is resonant diffraction anomalous fine structure (DAFS), which enables multimetallic clusters to be probed on a metal site-specific basis. DAFS experiments are high-resolution multiwavelength anomalous diffraction (MAD) measurements that depend on dramatic responses at the metal K-edge of anomalous scattering contributions to X-ray diffraction from single crystals, i.e., samples in which metal atoms have precisely determined spatial coordinates and thermal parameters. The resonant K-edge energies for each metal within even a homometallic cluster can differ slightly from each other, particularly regarding spectral fine structure, as evident from refinement of the real (f') and imaginary (f'') components of each atomic scattering factor as functions of incident X-ray photon energy. Thus, for homometallic clusters, DAFS can be viewed as a site-specific alternative to X-ray

absorption near-edge structure (XANES) spectroscopy, which also probes atomic X-ray resonances but only provides ensemble rather than site-specific data for multimetallic systems. Following early resonant diffraction studies on molecular clusters by Coppens,^{4–6} Einsle and Rees have used DAFS analysis to assign redox states of individual iron sites within a $2Fe:2S$ ferredoxin cluster,⁷ a mononuclear Fe site within the nitrogenase FeMo protein,⁸ and the $Mo:7Fe:9S:C$ cofactor (FeMoco) of nitrogenase.⁹ More recently, synthetic multinuclear clusters have been probed by DAFS at the Cr,¹⁰ Mn,¹¹ Fe,^{12,13} and Co¹⁴ K-edges to gain site-specific electronic structure data.

Leveraging our groups' expertise in synthesizing well-defined Cu clusters,^{15–25} here, we report the first documented DAFS experiments at the Cu K-edge. During our survey of different Cu-containing complexes using DAFS analysis, we discovered a case where individual Cu(I) ions within a tricopper(I) cluster are site-differentiated due to the presence of a nearby K^+ cation and its associated electrostatic field. The influence of cationic

Received: July 19, 2023

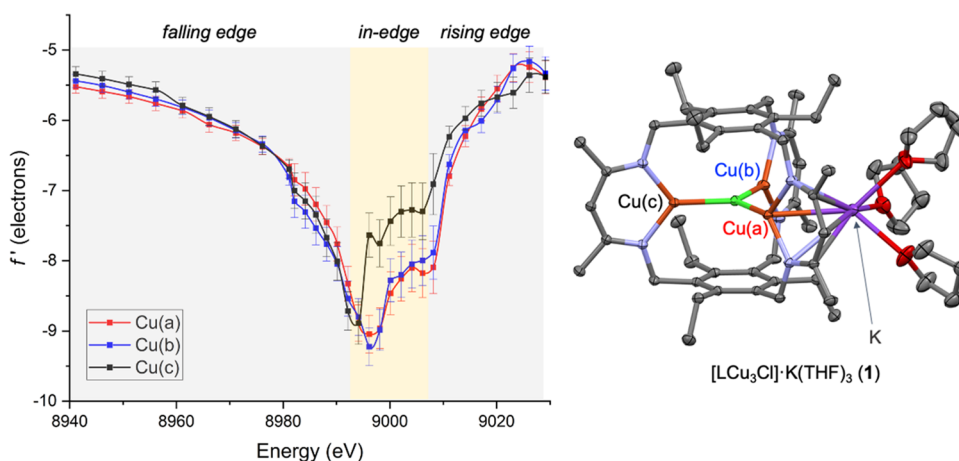


Figure 1. (left) Experimentally determined energy dependence of the f' scattering factor for each of the three Cu sites in $[\text{LCu}_3\text{Cl}]\cdot\text{K}(\text{THF})_3$ (**1**) and (right) crystal structure of **1**. Non-hydrogen atoms are shown as thermal ellipsoids (50% probability), and C–H hydrogens are omitted for clarity.

Table 1. Summary of Cu Complexes Studied

Cu complex	formal charge	coordination numbers ^a	coordination geometry ^a	ligand shell
$[\text{LCu}_3\text{Cl}]\cdot\text{K}(\text{THF})_3$ (1)	1	3	trigonal planar (C_{2v})	N_2Cl
	1	3	trigonal planar (C_{2v})	N_2Cl
	1	3	trigonal planar (C_{2v})	N_2Cl
$[\text{Cu}(\text{CH}_3\text{CN})_4][\text{BF}_4]$ (2)	1	4	tetrahedral (T_d)	N_4
$(\text{Ph}_3\text{P})_3\text{CuCl}$ (3)	1	4	pseudotetrahedral (C_{3v})	P_3Cl
$(\text{Ph}_3\text{P})_2\text{CuCl}$ (4)	1	3	trigonal planar (C_{2v})	P_2Cl
$\text{Cu}_2(\mu\text{-Cl})_2(\text{PPh}_3)_3$ (5)	1	4	pseudotetrahedral (C_{2v})	P_2Cl_2
	1	3	trigonal planar (C_{2v})	P_2Cl
$\text{Cu}_2(\text{NNN})_2$ (6)	1	3	t-shaped (C_{2v})	N_2Cu
$[\text{DABCO}\cdot 2\text{H}][\text{CuCl}_4]$ (7)	2	4	tetrahedral (T_d)	Cl_4
$[\beta\text{-alanine}\cdot\text{H}]_2[\text{CuCl}_4]$ (8)	2	4	square planar (D_{4h})	Cl_4
$\text{Cu}_2(\text{OAc})_4\cdot 2\text{H}_2\text{O}$ (9)	2	6	pseudooctahedral (C_{4v})	O_5Cu
$[\text{Cu}_3\text{S}(\text{dcpm})_3][\text{PF}_6]$ (10)	1	3	trigonal planar (C_{2v})	P_2S
	1	3	trigonal planar (C_{2v})	P_2S
	1	3	trigonal planar (C_{2v})	P_2S

^aThe coordination number and geometry are defined by including all neighboring atoms within covalent radius contact, including Cu atoms.

field effects on catalytic sites is an active area of investigation,^{26–30} with ramifications on various energy storage and conversion schemes as well as fundamental understanding of both heterogeneous catalysts^{31–33} and bioinorganic systems.^{34–36}

RESULTS AND DISCUSSION

The complex, $[\text{LCu}_3\text{Cl}]\cdot\text{K}(\text{THF})_3$ (**1**, L = trinucleating cyclophanate),¹⁸ contains a D_{3h} -symmetric, formally $3\text{Cu}(\text{I})$ cluster with a uniform ligand shell surrounding the three Cu(I) sites. Just based on these facts, one would expect all of the three Cu(I) centers' f' vs E plots to coincide with one another. Surprisingly, analysis of **1** by DAFS revealed that, although the f' traces for the three Cu(I) sites bear similarities, $f'[\text{Cu}(\text{a})]$ and $f'[\text{Cu}(\text{b})]$ were found to be blue-shifted in the right-hand rising (9008–9029 eV) edges, departing from the $f'[\text{Cu}(\text{c})]$ profile in this region (Figure 1). For this and all compounds in the study, plots of f'' vs E are given as Supporting Information.

Since there have been no DAFS studies conducted at the Cu K-edge prior to this work, we began our analysis by applying this experimental technique to strategically selected Cu(I) and Cu(II) reference crystals for analysis of emerging trends, with the ultimate goal of understanding the peculiar trend seen for **1**

and extracting local electronic structure information for individual Cu(I) sites in this cluster. The complexes that were analyzed successfully are summarized in Table 1. Neighboring Cu atoms were included in a given metal's ligand shell (and therefore the coordination number and geometry) if and only if $d(\text{Cu}\cdots\text{Cu})$ fell below the sum of two Cu covalent radii (2.64 Å).³⁷ The f'_{min} value was originally used by Coppens to assign site-specific oxidation states and showed a dependence of 4.6 eV per oxidation state unit at the Fe K-edge.⁶ However, more recent work by Betley on highly covalent Fe complexes indicates that broadening and complex fine structure renders f'_{min} to not necessarily be reflective of the local oxidation state.¹² Rather, subtle effects in the falling edge, in-edge, and rising edge regions (see Figure 1) must be analyzed holistically to gain useful interpretations.¹⁰ Similarly subtle analysis is required for Cu K-edge DAFS, as described below.

Coordination Influences. It has been well documented both in XANES studies at the Mn,³⁸ Fe,³⁹ and Cu^{40–43} K-edges as well as the earlier DAFS measurements at the Fe^{8,9,12,13} and Cr¹⁰ K-edges that coordination geometries of metal sites influence the spectral profiles and must be taken into account in addition to the oxidation state. To probe

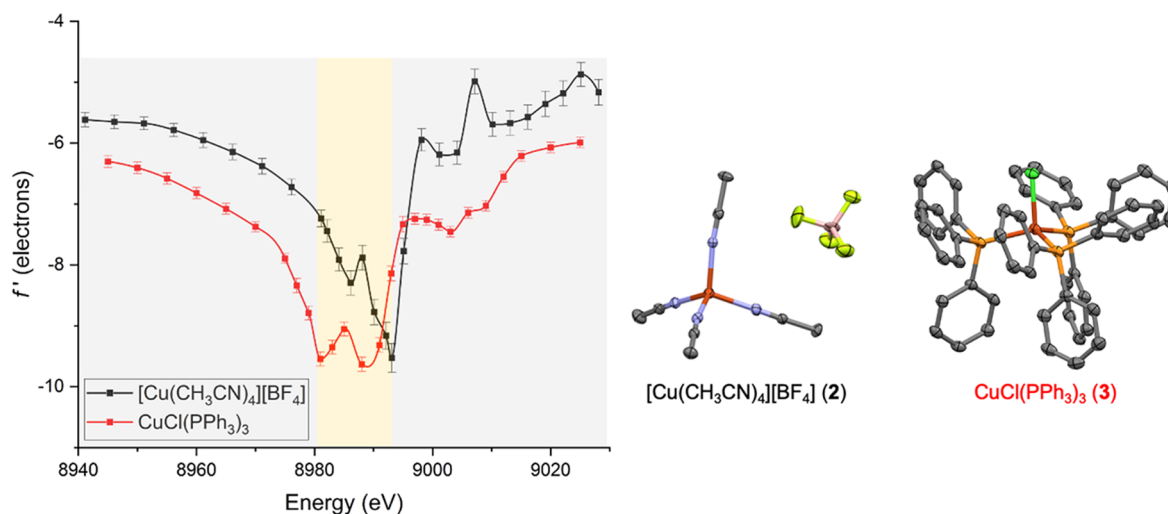


Figure 2. (left) Experimentally determined energy dependence of the f' scattering factor for $[\text{Cu}(\text{CH}_3\text{CN})_4][\text{BF}_4]$ (**2**) and $\text{CuCl}(\text{PPh}_3)_3$ (**3**) and (right) crystal structures of **2** and **3**. Non-hydrogen atoms are shown as thermal ellipsoids (50% probability), and C–H hydrogens are omitted for clarity. For **2**, data for only one of three molecules from the asymmetric unit are shown.

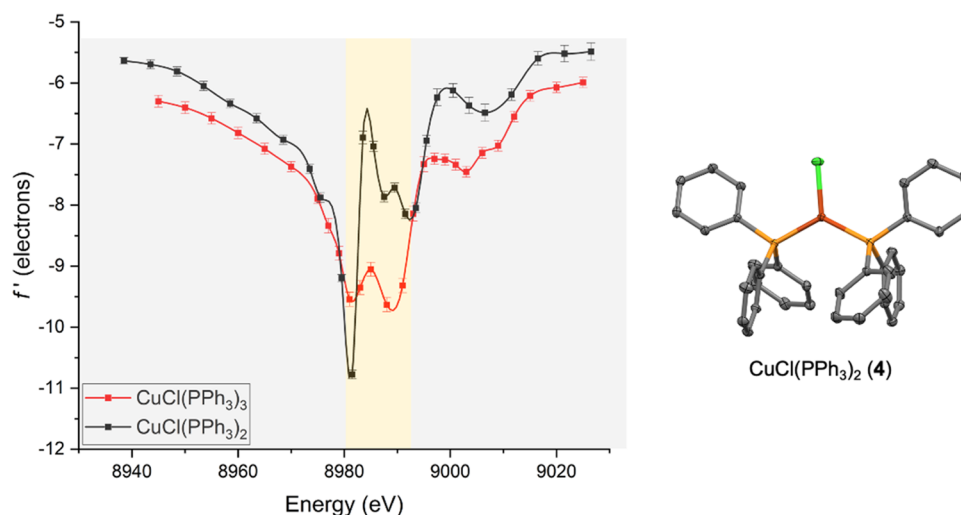


Figure 3. (left) Experimentally determined energy dependence of the f' scattering factor for $\text{CuCl}(\text{PPh}_3)_3$ (**3**) and $\text{CuCl}(\text{PPh}_3)_2$ (**4**) and (right) crystal structure of **4**. Non-hydrogen atoms are shown as thermal ellipsoids (50% probability), and C–H hydrogens are omitted for clarity.

coordination geometry and ligand shell effects on Cu K-edge DAFS, five different Cu(I) reference crystals were employed for analysis. The Cu(I) reference compounds were chosen based on coordination, nuclearity, and symmetry of the Cu(I) sites. Four of these references are mononuclear complexes with different coordination numbers and ligand shells: $[\text{Cu}(\text{CH}_3\text{CN})_4][\text{BF}_4]$ (**2**),^{44,45} $\text{CuCl}(\text{PPh}_3)_3$ (**3**),^{46,47} and $\text{CuCl}(\text{PPh}_3)_2$ (**4**).^{48,49} Comparison of **2** vs **3** probes influence of the ligand shell, i.e., *N*- vs *P*-ligation, with constant geometry. Comparison of **3** vs **4** probes influence of coordination geometry, i.e., trigonal planar vs tetrahedral, with constant PPh_3 ligand shells. The other two Cu(I) reference compounds are binuclear complexes: $\text{Cu}_2(\mu\text{-Cl})_2(\text{PPh}_3)_3$ (**5**)⁴⁸ and $\text{Cu}_2(\text{NNN})_2$ (**6**, $\text{NNN} = 1,3\text{-bis}(2,4,6\text{-trimethylphenyl})\text{-triazene}$).⁵⁰ Complex **5** contains both three- and four-coordinate, *P*-ligated sites for comparison to **3** and **4**. Complex **6** is symmetrical with identical, three-coordinate sites.

Both tetrakis(acetonitrile)copper(I) cation (**2**) and chlorotris(triphenylphosphine)copper(I) (**3**) exhibit (pseudo)-tetrahedral geometries. The sample of **2** was found to

crystallize with three independent molecules in the asymmetric unit, thus allowing us to refine the scattering factors for all three Cu sites independently (Figure S1). The three f' vs E plots for these three independent molecules are nearly identical in terms of both the peak shape and peak position, albeit with minor differences in f' amplitude, and only one plot is shown in Figure 2 along with that for **3**. Clearly, coordination environment-dependent differentiation in f' vs E in-edge peak shapes is observed for T_d -symmetric **2** vs C_{3v} -symmetric **3**. Complex **2** shows an asymmetrical “double dip” pattern with local and global f' minima at 8993 and 8986 eV, respectively. The resulting amplitude-weighted f'_{center} for **2** is positioned at about 8990 eV. In contrast, complex **3** has a symmetrical double dip pattern centered at about 8985 eV with f' minima at 8981 and 8988 eV. The f' trace for **2** is shifted to higher energy by approximately 9 and 3 eV in the falling edge (8940–8985 eV) and rising edge (8988–8998 eV) regions, respectively. The net result is that the f' peak for **3** with a softer ligand shell is broader and spans a larger energy envelope than that for **2** with the harder ligand shell. Such peak

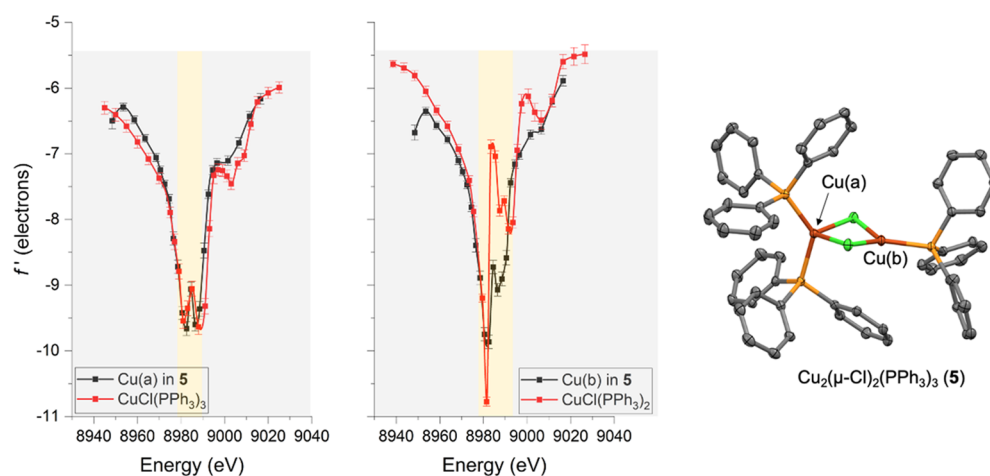


Figure 4. (left) Experimentally determined energy dependence of the f' scattering factor for the two Cu sites in $\text{Cu}_2(\mu\text{-Cl})_2(\text{PPh}_3)_3$ (**5**) each compared to its mononuclear analogue and (right) crystal structure of **5**. Non-hydrogen atoms are shown as thermal ellipsoids (50% probability), and C–H hydrogens are omitted for clarity.

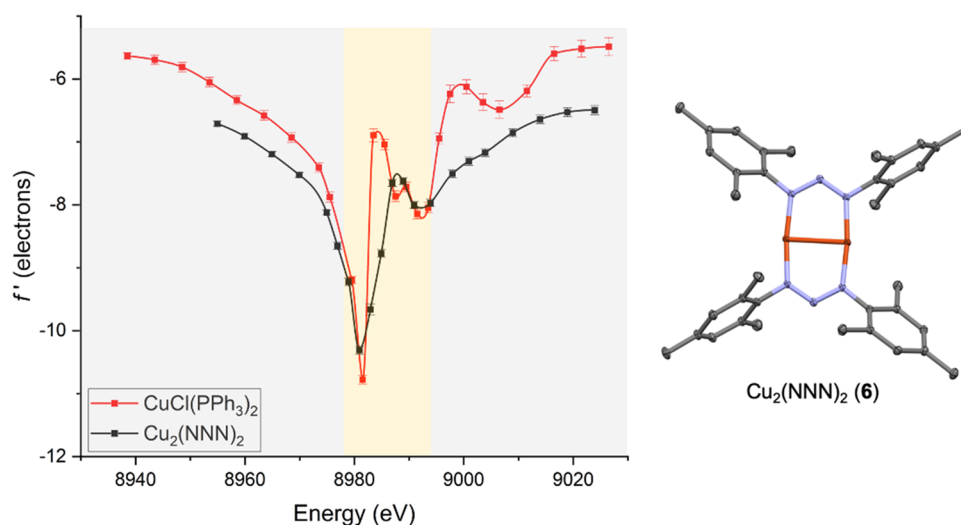


Figure 5. (left) Experimentally determined energy dependence of the f' scattering factor for $\text{CuCl}(\text{PPh}_3)_2$ (**4**) and $\text{Cu}_2(\text{NNN})_2$ (**6**, NNN = MesN–N=NMe) and (right) the crystal structure of **6**. Non-hydrogen atoms are shown as thermal ellipsoids (50% probability), and C–H hydrogens are omitted for clarity.

broadening has been observed before by Betley when comparing DAFS responses for $\text{Fe}_3(\mu_3\text{-Cl})$ and $\text{Fe}_3(\mu_3\text{-NPh})$ complexes and for related Cr_3 complexes and was attributed to metal–ligand covalency.^{10,12}

Three important aspects emerge from comparing DAFS responses of **2** and **3**. First, the breadth of the f' energy envelope for **2** vs **3** reflects the relative copper–ligand covalency. Second, the different peak shapes for **2** vs **3** can be attributed to changes in the coordination environment.^{40,43} The physical origin of the DAFS in-edge features is unclear, and so currently the peak shapes can be used simply as “fingerprints” for different coordination geometries. Third, the peak position for **2** is definitively shifted to higher energy than those of **3** and **4** (*vide infra*) whether analyzing the falling edge, rising edge, or f'_{min} positions. The shift to higher energy is presumably correlated to the weaker donor properties of CH_3CN compared to PPh_3 , leading to a slightly higher effective nuclear charge (Z_{eff}) for the Cu(I) center in **2** compared to **3**.

To focus only on geometry effects while eliminating the ligand shell influence, chlorobis(triphenylphosphine)copper(I) (**4**)⁵¹ was also studied for comparison to **3** (Figure 3). Complex **4** exhibits a sharp f' minimum at 8981 eV and as such represents the lowest f'_{min} energy in this study. There is also a weak local minimum at about 8993 eV, just below the rising edge. The falling edge for **4** is shifted to higher energy by 3.5 eV compared to **3**, whereas the rising edge for **4** is shifted to lower energy by 1.5 eV compared to **3**. The result is that the overall energy envelope for **4** is slightly narrower than that of **3**. The f'_{min} and amplitude-weighted f'_{center} values for **4** are lower in energy than the amplitude-weighted f'_{center} of **3** by approximately 3–4 eV. This turns out to be a general trend across all complexes examined, with f' features for three-coordinate Cu(I) sites (**4**, **5**, and **6**) being shifted to lower energy by 3–4 eV than four-coordinate Cu(I) sites (**2**, **3**, and **5**). This energy shift due to coordination number is in accord with the previously reported XANES studies of Cu(I) complexes.^{40,42,43}

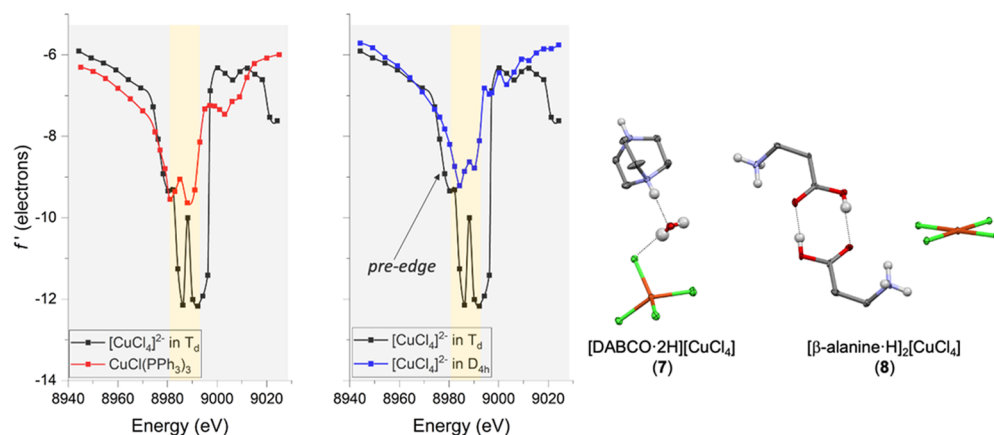


Figure 6. (left) Experimentally determined energy dependence of the f' scattering factor for $[\text{CuCl}_4]^{2-}$ in T_d symmetry (7) compared to $\text{CuCl}(\text{PPh}_3)_3$ (3) and $[\text{CuCl}_4]^{2-}$ in D_{4h} symmetry (8) and (right) crystal structures of 7 and 8. Non-hydrogen atoms are shown as thermal ellipsoids (50% probability), and C–H hydrogens are omitted for clarity. Error bars were omitted from f' refinement for clarity and are shown in the Supporting Information.

As for the binuclear member of the Cu(I)-phosphine series, cluster 5, the f' vs E trace for each Cu site appears roughly superimposable with its mononuclear analogue in 3 and 4 in terms of the in-edge features (Figure 4). However, the overall f' envelopes for the four-coordinate Cu(a) and three-coordinate Cu(b) sites in 5 cover different ranges compared to the corresponding mononuclear Cu(I)-phosphine sites. In the falling edge region (8950–8981 eV), both 3 and the Cu(a) site in 5 exhibit roughly overlapping f' traces. Yet, the plots diverge in the rising edge region (8988–9003 eV), with the f' trace for Cu(a) in 5 being shifted 2 eV lower in energy than that of 3. Therefore, Cu(a) in 5 exhibits a slightly narrower f' profile than 3. A similar pattern is seen when comparing the Cu(b) site in 5 with mononuclear 4: the falling edge regions overlay, whereas the rising edge for Cu(b) in 5 is red-shifted prior to a crossing point at 8994 eV, giving Cu(b) in 5 a slightly narrower linewidth than 4. This peak narrowing can be attributed to complex 5 being less covalent than mononuclear analogues 3 and 4 due to its lower P/Cl ratio at each copper site. It is also possible that cluster nuclearity plays a role in modulating peak width and/or position due to a given Cu site experiencing the electrostatic field of the other, but more data are required to study such phenomena rigorously. Importantly, the in-edge features of the two Cu sites in binuclear 5 can be traced back to their mononuclear analogues, underscoring the connection between the f' peak shape and coordination geometry.

The last binuclear Cu(I) reference employed here was $\text{Cu}_2(\text{NNN})_2$ (6). The choice of this reference was twofold: to compare/contrast the T-shaped (6) vs trigonal planar (4) three-coordinate geometries and to probe how different ligand shell environments influence the f' vs E plots. It is important to note that binuclear 6 crystallized with only one independent Cu(I) site in the asymmetric unit. Thus, only one f' plot is shown in Figure 5. The f' profile has a global minimum positioned at 8981 eV with a weak local minimum at 8991 eV, thus showing an overall peak shape that is very similar to the one for trigonal planar 4. Although the in-edge features are similar, the falling and rising edges differentiate. In the left-hand falling edge portion of the spectrum, the f' trace for 4 is blue-shifted, whereas in the right-hand rising edge region the f' trace is red-shifted. As a result, binuclear 6 has a broader f' energy envelope than mononuclear 4. This broadening

observed for 6 is reflective of differences in metal–ligand covalency, as mentioned above.

Oxidation Influence. Three Cu(II) standards were chosen. First, tetrachlorocuprate ($[\text{CuCl}_4]^{2-}$) was analyzed in two different coordination geometries as a function of counteraction: the $[\text{DABCO-2H}][\text{CuCl}_4]$ salt (7) contains a Cu(II) site with local T_d symmetry⁵² and the $[\beta\text{-alanine}]_2[\text{CuCl}_4]$ salt (8) contains a Cu(II) site with local D_{4h} symmetry.⁵³ Lastly, $\text{Cu}_2(\text{OAc})_4 \cdot 2\text{H}_2\text{O}$ (9) was used as a binuclear Cu(II) standard; both Cu(II) centers feature six-coordinate, pseudo-octahedral (C_{4v}) environments when including the neighboring Cu atom.

Initially, the f' vs E profile for tetrahedral Cu(II) complex 7 can be compared to those for (pseudo)tetrahedral Cu(I) complexes 2 and 3 to examine the oxidation effect without changing geometry. As expected, the peak shape of 7 (Figure 6) resembles those of 2 and 3 with a double dip pattern but with f_{min} values of 8986 and 8992 eV that are blue-shifted by 3–5 eV compared to the Cu(I) analogues. In the left-hand falling edge region (8940–8986 eV), f' for 7 is shifted to lower energy by 5 eV than for 2. The order is reversed in the right-hand rising edge region (8993–9003 eV), which shows a blue shift of 3 eV for 7 compared to 2. The blue shift for 7 increases to 5 eV in the rising edge region when compared to 3, which is a more electron-rich Cu(I) complex than 2. Compared to complex 3, complex 7 is also blue-shifted in the falling edge region. Therefore, we can conclude that oxidation of a Cu site with constant coordination geometry generally yields higher energy f' vs E profiles.

Though f' profiles of 7 and 8 fall within the same energy envelope, they exhibit some differences (Figure 6). The D_{4h} analogue 8 displays a slightly asymmetric f' peak shape, with minima at 8984 and 8990 eV. A pre-edge feature for the forbidden $1s \rightarrow 3d$ transition is not evident in the f' plot of 8 but is observed for 7 at ~8980 eV. In the falling edge region (8940–8974 eV), the f' traces for 7 and 8 are superimposed. After 8974 eV, they begin to diverge, with f' for 8 shifted 4 eV higher in energy than 7. This order is inverted in the rising edge region (8990–8997 eV), with f' for 8 tracing 4 eV lower than 7. These changes as a function of coordination geometry parallel the effects observed for Cu(I) references discussed above and agree with XANES studies probing the Cu(II) complexes.^{40,42,43,54,55}

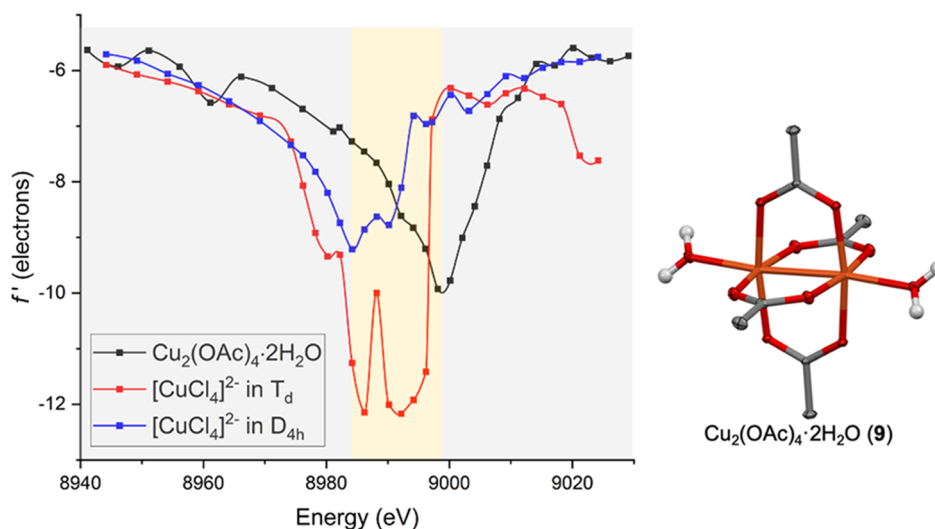


Figure 7. (left) Experimentally determined energy dependence of the f' scattering factor for $\text{Cu}_2(\text{OAc})_4 \cdot 2\text{H}_2\text{O}$ (**9**) compared to $[\text{CuCl}_4]^{2-}$ in T_d (**7**) D_{4h} (**8**) symmetry and (right) crystal structure of **9**. Non-hydrogen atoms are shown as thermal ellipsoids (50% probability), and C–H hydrogens are omitted for clarity. Error bars were omitted from f' refinement for clarity and are shown in the [Supporting Information](#).

The binuclear, six-coordinate Cu(II) analogue, **9**, crystallizes with only one Cu center in its asymmetric unit. The resulting single f' vs E plot shows an asymmetric dip centered at 8998 eV and as such has the highest energy (global) f'_{\min} of all of the complexes in this study (Figure 7). Within the Cu(II) batch, six-coordinate **9** displays an f' profile shifted to higher energy than its lower-coordinate Cu(II) counterparts (**7** and **8**), which is consistent with the XANES literature on coordination geometry effects^{40,41,43} and with the pattern seen for Cu(I) compounds discussed above. While the f'_{\min} for **9** matches with the global minima for the Cu(a) and Cu(b) sites in **1**, Table 1, the direct comparison of f' energies between **1** and **9** would be misleading because the Cu sites differ in their oxidation levels, ligand shells, and coordination numbers/geometries of the Cu sites, all of which influence the f' peak shape and position. Hence, in agreement with the previous DAFS literature,^{10,12} the absolute f'_{\min} values will not be interpreted to probe the oxidation state effects as they are strongly influenced by the in-edge features, which in turn are sensitive to the ligand shell and the local geometry at the copper center. Instead, a comparison of falling and rising edges and the resulting energy envelope proves to be a more reliable diagnostic tool to probe the oxidation state at a Cu site when considering all data discussed thus far.

Summary of Trends from Mono- and Binuclear Samples. Several trends can be summarized from the above analyses of complexes **2–9**. The following trends can be viewed as independent of Z_{eff} :

- Similar Cu(I) coordination geometries give similar fingerprints in terms of the f' in-edge peak shape.
- Increasing coordination number tends to shift the apparent f' energy envelope to higher energy by ~ 4 eV per ligand.
- Enhanced metal–ligand covalency increases the breadth/span of the f' energy envelope.

When controlling for coordination geometry and coordination number, the following effects from changes in Z_{eff} are observed, particularly in the rising edge region:

- Electron-rich ligands shift f' to lower energy.

- Oxidation from Cu(I) to Cu(II) shifts f' to higher energy by $\sim 3–5$ eV

Tricopper Clusters. Upon having examined how the coordination geometries, ligand shell, and oxidation level influence the f' vs E profiles as systematically as possible, we revisited the peculiar trend observed in the f' plots for the three individual metal sites of the D_{3h} symmetric, formally all-cuprous, $[\text{LCu}_3\text{Cl}]\cdot\text{K}(\text{THF})_3$ (**1**). All three Cu sites in **1** exhibit very similar in-edge spectral features, yet they are distinct in both the left-hand falling edge (8940–8994 eV) and right-hand rising edge (9008–9029 eV) regions, with Cu(a) and Cu(b) resembling each other and Cu(c) appearing unique (Figure 1). In the f' falling edge region, the three Cu sites are separated by 2–3 eV each, with Cu(a) falling between Cu(b) and Cu(c). In the f' rising edge region, energies for Cu(a) and Cu(b) are shifted to 2 eV higher energy than that of Cu(c). As shown above as well as in the previous DAFS studies on Co_6 ,¹⁴ Cr_3 ,¹⁰ and Fe_3 ¹² clusters and the mononuclear Fe site within the nitrogenase FeMo protein,⁸ the in-edge features in f' plots are highly responsive to the coordination number/geometry and the ligand shell. Since the D_{3h} -symmetric Cu_3 core is wrapped by a uniform ligand shell and all of the f' plots display matching features, we can eliminate the geometry and ligand shell influences as reasons for the f' profiles of Cu(a) and Cu(b) diverging from that of Cu(c). Instead, the observations are suggestive of Cu(a) and Cu(b) being more oxidized than Cu(c). Indeed, the pattern of Cu(a) and Cu(b) blue-shifting in the rising edge region parallels the pattern seen when comparing tetrahedral Cu(II) complex **7** with tetrahedral Cu(I) complex **2**.

If the crystal structure of cluster **1** is examined closely (Figure 1), the effects leading to Cu site-specific oxidation are clear: the solid-state structure is unsymmetrical due to a proximal K^+ counteraction. Specifically, a $[\text{K}(\text{THF})_3]^+$ cation is seen to form an apparent cation– π interaction with the Cu(β -diketiminato) subunit containing Cu(a). The result is an array of three Cu \cdots K distances: Cu(a) \cdots K, 3.0881(7) Å; Cu(b) \cdots K, 4.3775(6) Å; and Cu(c) \cdots K, 6.4004(7) Å. There is also a small asymmetry of Cu–Cl distances, with the Cu(a) site closest to K^+ also having a shorter Cu–Cl distance

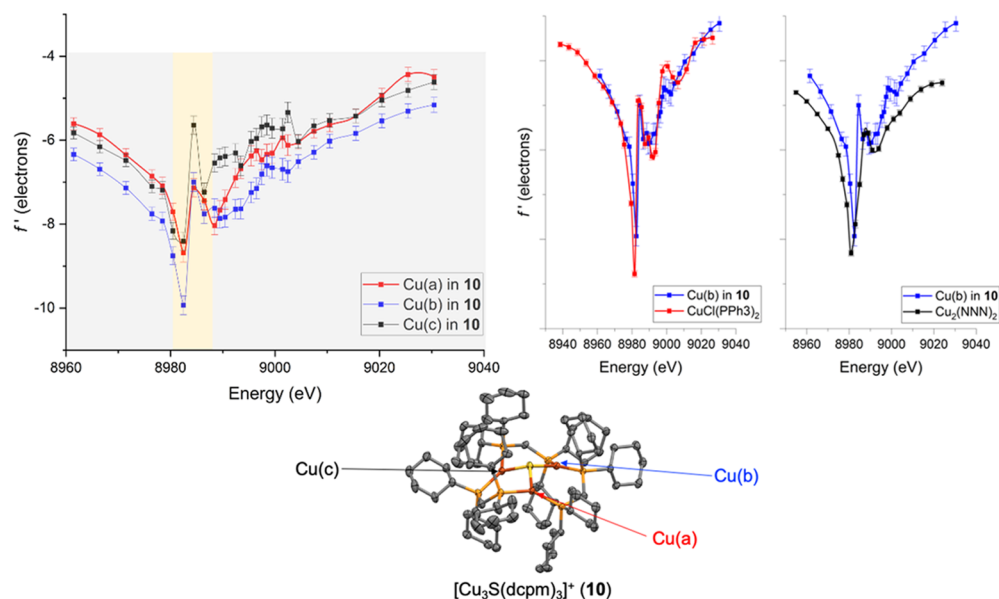


Figure 8. (top) Experimentally determined energy dependence of the f' scattering factor for the three Cu sites in $[\text{Cu}_3(\mu_3\text{-S})(\text{dcpm})_3][\text{PF}_6]$ (**10**) and comparison of the Cu(b) site to $\text{CuCl}(\text{PPh}_3)_2$ (**4**) and $\text{Cu}_2(\text{NNN})_6$ (**6**) and (bottom) the crystal structure of **10**. Non-hydrogen atoms are shown as thermal ellipsoids (50% probability), and C–H hydrogens and the counteranion are omitted for clarity.

(2.1679(5) Å) than the Cu(b) and Cu(c) sites (2.1905(5) and 2.1842(7) Å, respectively). The Cu(a) site also participates in shorter Cu...Cu distances [3.7648(4) and 3.6947(6) Å to Cu(b) and Cu(c), respectively] than the longer Cu(b)...Cu(c) cluster edge (3.8681(6) Å). This contraction of the Cu(a) center's covalent radius apparent from bond metrics is consistent with it being measurably oxidized. The fact that the Cu(a) and Cu(b) sites give effectively identical responses by Cu K-edge DAFS despite having measurably different distances to K^+ indicates that there is not any direct Cu(a)...K interaction to differentiate Cu(a) from Cu(b), which is consistent with their having nearly identical f' vs E peak shapes. Instead, it is likely that both Cu(a) and Cu(b) are within the range to experience an electrostatic field effect from the K^+ cation. The Cu(c) site, on the other hand, is sufficiently far away from K^+ that it does not experience this field effect. Therefore, the proximity of a Cu(I) site to K^+ serves to slightly increase its Z_{eff} with the outer limit of that electric field effect being somewhere between 4.4 and 6.4 Å of the Cu...K distance. Though effects of alkali metal cations on transition-metal sites in well-defined coordination complexes have been probed electrochemically,^{26,27,56} only recently has there been a XPS study on an iron(III) complex with an alkaline earth metal binding site in the second coordination sphere.⁵⁷ The data in that study were also consistent with decreased electron density at iron(III) when in proximity to an alkaline earth metal cation. Like in the case of **1**, analysis of this Fe...M system by QTAIM indicated a lack of metal–metal bond. Otherwise, to the best of our knowledge, there has not been a previous study of metal site-specific electrostatic field effects by X-ray spectroscopy prior to our work.

As a control experiment, $[\text{Cu}_3(\mu_3\text{-S})(\text{dcpm})_3][\text{PF}_6]$ (**10**) was analyzed by DAFS (dcpm = 1,3-bis-(dicyclohexylphosphino)methane). Although the ligand shell supporting the tricopper(I) core in **10** is different from that of **1**, nonetheless **10** is also a formally all-cuprous, C_3 -symmetric tricopper cluster but lacks the K^+ cation seen in the solid-state structure of **1**. Moreover, both clusters feature three-coordinate

Cu sites with uniform ligand shells and comparable Cu...Cu distances (3.5684(3)–3.6753(3) Å for **10**).²⁰ Therefore, tricopper(I) cluster **10** provides an opportunity to probe if the polarization observed for **1** is, indeed, introduced by K^+ proximity. As initially expected for a formally 3Cu(I) cluster, the DAFS analysis of **10** yielded three f' vs E profiles each spanning the same energy envelope (Figure 8). Each f' trace showed very similar in-edge features due to the homogeneity of coordination shells at the three metal sites. Moreover, the site-specific f' profiles for **10** exhibited a sharp dip feature matching the peak shape for trigonal planar Cu(I) reference, $\text{CuCl}(\text{PPh}_3)_2$ (**4**, Figure 8) due to comparable coordination geometries, ligand environments, and oxidation states. Although at first glance it appears as if the Cu(b) site covers a wider energy span than the Cu(a) and Cu(c) sites in **10**, this is mainly due to a change in f' amplitude. A similar effect was observed when comparing the three crystallographically independent $[\text{Cu}(\text{CH}_3\text{CN})_4]^+$ cations in **2** (see Figure S1). Moreover, the entire energy envelope spanned by the Cu(b) site still falls completely inside that of $\text{Cu}_2(\text{NNN})_2$ (**6**, Figure 8). Therefore, effectively, the three f' traces for **10** span the same energy envelope as each other due to uniform redox delocalization across the Cu_3S core, like the three unique $[\text{Cu}(\text{CH}_3\text{CN})_4]^+$ sites in **2** but unlike the Cu_3Cl core of **1**. All of these observations suggest that, if the K^+ proximity to the Cu_3Cl core could be avoided for **1**, its three f' profiles would collapse to a single energy envelope. Unfortunately, attempts to analyze analogues of **1** with crown ether encapsulation of K^+ or through use of alternative cations did not yield samples suitable for DAFS.

CONCLUSIONS

Cu K-edge DAFS analysis was applied to strategically chosen Cu(I) and Cu(II) complexes to probe how the energy dependencies of the anomalous scattering term, f' , are influenced by coordination geometry, ligand environment, cluster nuclearity, and metal oxidation state. In agreement with the previous DAFS studies,^{10,12} the complexes analyzed here

indicate that in-edge f' features are highly sensitive to coordination geometries: not only does the coordination geometry influence the peak shape but also the coordination number impacts the peak position to an extent comparable to the oxidation state (akin to Cu K-edge XANES^{40,42,43}). When controlling for these factors, blue shifts in f' vs E traces are seen upon replacement of electron-rich ancillary ligands (e.g., PPh₃) with electron-poor ones (e.g., CH₃CN) or upon oxidation of Cu(I) to Cu(II). Considering these calibration studies, site differentiation within a tricopper(I) cluster (1) due to the electrostatic field of a proximal K⁺ ion was detected by Cu K-edge DAFS, with the dominant effect being an increase in effective oxidation state for Cu centers near the K⁺ cation. Unlike techniques such as electrochemistry that probe cationic field effects on an entire molecule or bulk material, this study provides complementary data showing unsymmetrical effects of a cationic field on individual metal sites within a cluster.

■ ASSOCIATED CONTENT

SI Supporting Information

The Supporting Information is available free of charge at <https://pubs.acs.org/doi/10.1021/acs.inorgchem.3c02472>.

The following files are available free of charge. Synthetic procedures, X-ray diffraction refinement details, and additional data plots (PDF)

Accession Codes

CCDC 2235253–2235254, 2235257–2235258, 2235433, 2235448, 2235477, 2270005–2270006, and 2270325 contain the supplementary crystallographic data for this paper. These data can be obtained free of charge via www.ccdc.cam.ac.uk/data_request/cif, or by emailing data_request@ccdc.cam.ac.uk, or by contacting The Cambridge Crystallographic Data Centre, 12 Union Road, Cambridge CB2 1EZ, UK; fax: +44 1223 336033.

■ AUTHOR INFORMATION

Corresponding Author

Neal P. Mankad – Department of Chemistry, University of Illinois at Chicago, Chicago, Illinois 60607, United States; orcid.org/0000-0001-6923-5164; Email: npm@uic.edu

Authors

Pinar Alayoglu – Department of Chemistry, University of Illinois at Chicago, Chicago, Illinois 60607, United States
Tieyan Chang – ChemMatCARS, The University of Chicago, Argonne, Illinois 60439, United States
M. Victoria Lorenzo Ocampo – Center for Catalysis and Florida Center for Heterocyclic Chemistry, Department of Chemistry, University of Florida, Gainesville, Florida 32611, United States
Leslie J. Murray – Center for Catalysis and Florida Center for Heterocyclic Chemistry, Department of Chemistry, University of Florida, Gainesville, Florida 32611, United States; orcid.org/0000-0002-1568-958X
Yu-Sheng Chen – ChemMatCARS, The University of Chicago, Argonne, Illinois 60439, United States

Complete contact information is available at: <https://pubs.acs.org/doi/10.1021/acs.inorgchem.3c02472>

Author Contributions

The manuscript was written through contributions of all authors. All authors have given approval to the final version of the manuscript.

Notes

The authors declare no competing financial interest.

■ ACKNOWLEDGMENTS

This project was funded by NIH (R35 GM140850 to N.P.M.) and DOE (DE-SC0022174 to L.J.M.). P.A. was supported by a Moriarty Graduate Fellowship from the UIC Department of Chemistry. NSF's ChemMatCARS Sector 15 is supported by the Divisions of Chemistry (CHE) and Materials Research (DMR), National Science Foundation, under grant number NSF/CHE-1834750. Use of the Advanced Photon Source, an Office of Science User Facility operated for the U.S. Department of Energy (DOE) Office of Science by Argonne National Laboratory, was supported by the U.S. DOE under Contract No. DE-AC02-06CH11357.

■ REFERENCES

- (1) Wang, Z.; She, X.; Yu, Q.; Zhu, X.; Li, H.; Xu, H. Minireview on the Commonly Applied Copper-Based Electrocatalysts for Electrochemical CO₂ Reduction. *Energy Fuels* **2021**, *35*, 8585–8601.
- (2) Murthy, P. S.; Liang, W.; Jiang, Y.; Huang, J. Cu-Based Nanocatalysts for CO₂ Hydrogenation to Methanol. *Energy Fuels* **2021**, *35*, 8558–8584.
- (3) Solomon, E. I.; Heppner, D. E.; Johnston, E. M.; Ginsbach, J. W.; Cirera, J.; Qayyum, M.; Kieber-Emmons, M. T.; Kjaergaard, C. H.; Hadt, R. G.; Tian, L. Copper Active Sites in Biology. *Chem. Rev.* **2014**, *114*, 3659–3853.
- (4) Gao, Y.; Frost-Jensen, A.; Pressprich, M. R.; Coppens, P.; Marquez, A.; Dupuis, M. Valence Contrast by Synchrotron Resonance Scattering: Application to a Mixed-Valence Manganese Compound. *J. Am. Chem. Soc.* **1992**, *114*, 9214–9215.
- (5) Gao, Y.; Pressprich, M. R.; Coppens, P. Anomalous-scattering Contrast Study of the Mixed-valence Charge-density-wave Conductor NbSe₃. *Acta Crystallogr., Sect. A: Found. Crystallogr.* **1993**, *49*, 216–219.
- (6) Wu, G.; Zhang, Y.; Ribaud, L.; Coppens, P.; Wilson, C.; Iversen, B. B.; Larsen, F. K. Multitemperature Resonance-Diffraction and Structural Study of the Mixed-Valence Complex [Fe₃O(OOCC(CH₃)₃)₆(C₅H₅N)₃]. *Inorg. Chem.* **1998**, *37*, 6078–6083.
- (7) Einsle, O.; Andrade, S. L. A.; Dobbek, H.; Meyer, J.; Rees, D. C. Assignment of Individual Metal Redox States in a Metalloprotein by Crystallographic Refinement at Multiple X-Ray Wavelengths. *J. Am. Chem. Soc.* **2007**, *129*, 2210–2211.
- (8) Zhang, L.; Kaiser, J. T.; Meloni, G.; Yang, K. Y.; Spatzal, T.; Andrade, S. L. A.; Einsle, O.; Howard, J. B.; Rees, D. C. The Sixteenth Iron in the Nitrogenase MoFe Protein. *Angew. Chem., Int. Ed.* **2013**, *52*, 10529–10532.
- (9) Spatzal, T.; Schlesier, J.; Burger, E.-M.; Sippel, D.; Zhang, L.; Andrade, S. L. A.; Rees, D. C.; Einsle, O. Nitrogenase FeMoco Investigated by Spatially Resolved Anomalous Dispersion Refinement. *Nat. Commun.* **2016**, *7*, No. 10902.
- (10) Bartholomew, A. K.; Musgrave, R. A.; Anderton, K. J.; Juda, C. E.; Dong, Y.; Bu, W.; Wang, S.-Y.; Chen, Y.-S.; Betley, T. A. Revealing Redox Isomerism in Trichromium Imides by Anomalous Diffraction. *Chem. Sci.* **2021**, *12*, 15739–15749.
- (11) Han, H.; Carozza, J. C.; Zhou, Z.; Zhang, Y.; Wei, Z.; Abakumov, A. M.; Filatov, A. S.; Chen, Y. S.; Santalucia, D. J.; Berry, J. F.; Dikarev, E. V. Hetero Trimetallic Precursor with 2:2:1 Metal Ratio Requiring at Least a Pentanuclear Molecular Assembly. *J. Am. Chem. Soc.* **2020**, *142*, 12767–12776.
- (12) Bartholomew, A. K.; Teesdale, J. J.; Sánchez, R. H.; Malbrecht, B. J.; Juda, C. E.; Ménard, G.; Bu, W.; Iovan, D. A.; Mikhailine, A. A.; Zheng, S. L.; Sarangi, R.; Wang, S. Y. G.; Chen, Y. S.; Betley, T. A.

Exposing the Inadequacy of Redox Formalisms by Resolving Redox Inequivalence within Isovalent Clusters. *Proc. Natl. Acad. Sci. U.S.A.* **2019**, *116*, 15836–15841.

(13) Arnett, C. H.; Kaiser, J. T.; Agapie, T. Remote Ligand Modifications Tune Electronic Distribution and Reactivity in Site-Differentiated, High-Spin Iron Clusters: Flipping Scaling Relationships. *Inorg. Chem.* **2019**, *58*, 15971–15982.

(14) Hernández Sánchez, R.; Champsaur, A. M.; Choi, B.; Wang, S. G.; Bu, W.; Roy, X.; Chen, Y. S.; Steigerwald, M. L.; Nuckolls, C.; Paley, D. W. Electron Cartography in Clusters. *Angew. Chem., Int. Ed.* **2018**, *57*, 13815–13820.

(15) Cook, B. J.; Di Francesco, G. N.; Ferreira, R. B.; Lukens, J. T.; Silberstein, K. E.; Keegan, B. C.; Catalano, V. J.; Lancaster, K. M.; Shearer, J.; Murray, L. J. Chalcogen Impact on Covalency within Molecular $[\text{Cu}_3(\mu_3\text{-E})_3]^+$ Clusters (E = O, S, Se): A Synthetic, Spectroscopic, and Computational Study. *Inorg. Chem.* **2018**, *57*, 11382–11392.

(16) Cook, B. J.; Di Francesco, G. N.; Kieber-Emmons, M. T.; Murray, L. J. A Tricopper(I) Complex Competent for O Atom Transfer, C–H Bond Activation, and Multiple O₂ Activation Steps. *Inorg. Chem.* **2018**, *57*, 11361–11368.

(17) Cook, B. J.; Di Francesco, G. N.; Abboud, K. A.; Murray, L. J. Counterions and Solvent Influence CO₂ Reduction to Oxalate by Chalcogen-Bridged Tricopper Cyclophanates. *J. Am. Chem. Soc.* **2018**, *140*, 5696–5700.

(18) Di Francesco, G. N.; Gaillard, A.; Ghiviriga, I.; Abboud, K. A.; Murray, L. J. Modeling Biological Copper Clusters: Synthesis of a Tricopper Complex, and Its Chloride- and Sulfide-Bridged Congeners. *Inorg. Chem.* **2014**, *53*, 4647–4654.

(19) Murray, L. J.; Weare, W. W.; Shearer, J.; Mitchell, A. D.; Abboud, K. A. Isolation of a (Dinitrogen)Tricopper(I) Complex. *J. Am. Chem. Soc.* **2014**, *136*, 13502–13505.

(20) Johnson, B. J.; Lindeman, S. V.; Mankad, N. P. Assembly, Structure, and Reactivity of Cu₄S and Cu₃S Models for the Nitrous Oxide Reductase Active Site, CuZ. *Inorg. Chem.* **2014**, *53*, 10611–10619.

(21) Johnson, B. J.; Antholine, W. E.; Lindeman, S. V.; Mankad, N. P. A Cu₄S Model for the Nitrous Oxide Reductase Active Sites Supported Only by Nitrogen Ligands. *Chem. Commun.* **2015**, *51*, 11860–11863.

(22) Johnson, B. J.; Antholine, W. E.; Lindeman, S. V.; Graham, M. J.; Mankad, N. P. A One-Hole Cu₄S Cluster with N₂O Reductase Activity: A Structural and Functional Model for CuZ. *J. Am. Chem. Soc.* **2016**, *138*, 13107–13110.

(23) Rathnayaka, S. C.; Islam, S. M.; Dimucci, I. M.; MacMillan, S. N.; Lancaster, K. M.; Mankad, N. P. Probing the Electronic and Mechanistic Roles of the M₄-Sulfur Atom in a Synthetic CuZ Model System. *Chem. Sci.* **2020**, *11*, 3441–3447.

(24) Rathnayaka, S. C.; Hsu, C. W.; Johnson, B. J.; Iniguez, S. J.; Mankad, N. P. Impact of Electronic and Steric Changes of Ligands on the Assembly, Stability, and Redox Activity of Cu₄(μ_4 -S) Model Compounds of the CuZ Active Site of Nitrous Oxide Reductase (N₂O). *Inorg. Chem.* **2020**, *59*, 6496–6507.

(25) Hsu, C.-W. W.; Rathnayaka, S. C.; Islam, S. M.; MacMillan, S. N.; Mankad, N. P. N₂O Reductase Activity of a [Cu₄S] Cluster in the 4CuI Redox State Modulated by Hydrogen Bond Donors and Proton Relays in the Secondary Coordination Sphere. *Angew. Chem., Int. Ed.* **2020**, *59*, 627–631.

(26) Kang, K.; Fuller, J.; Reath, A. H.; Ziller, J. W.; Alexandrova, A. N.; Yang, J. Y. Installation of Internal Electric Fields by Non-Redox Active Cations in Transition Metal Complexes. *Chem. Sci.* **2019**, *10*, 10135–10142.

(27) Tsui, E. Y.; Tran, R.; Yano, J.; Agapie, T. Redox-Inactive Metals Modulate the Reduction Potential in Heterometallic Manganese–Oxido Clusters. *Nat. Chem.* **2013**, *5*, 293–299.

(28) Pattanayak, S.; Loewen, N. D.; Berben, L. A. Using Substituted [Fe₄N(CO)₁₂][–] as a Platform To Probe the Effect of Cation and Lewis Acid Location on Redox Potential. *Inorg. Chem.* **2023**, *62*, 1919–1925.

(29) Shaik, S.; Ramanan, R.; Danovich, D.; Mandal, D. Structure and Reactivity/Selectivity Control by Oriented-External Electric Fields. *Chem. Soc. Rev.* **2018**, *47*, 5125–5145.

(30) Ciampi, S.; Darwish, N.; Aitken, H. M.; Díez-Pérez, I.; Coote, M. L. Harnessing Electrostatic Catalysis in Single Molecule, Electrochemical and Chemical Systems: A Rapidly Growing Experimental Tool Box. *Chem. Soc. Rev.* **2018**, *47*, 5146–5164.

(31) Shin, S.-J.; Choi, H.; Ringe, S.; Won, D. H.; Oh, H.-S.; Kim, D. H.; Lee, T.; Nam, D.-H.; Kim, H.; Choi, C. H. A Unifying Mechanism for Cation Effect Modulating C1 and C2 Productions from CO₂ Electroreduction. *Nat. Commun.* **2022**, *13*, No. 5482.

(32) Chapovetsky, A.; Kennedy, R. M.; Witzke, R.; Wegener, E. C.; Dogan, F.; Patel, P.; Ferrandon, M.; Niklas, J.; Poluektov, O. G.; Rui, N.; Senanayake, S. D.; Rodriguez, J. A.; Zaluzec, N. J.; Yu, L.; Wen, J.; Johnson, C.; Jenks, C. J.; Kropf, A. J.; Liu, C.; Delferro, M.; Kaphan, D. M. Lithium-Ion Battery Materials as Tunable, “Redox Non-Innocent” Catalyst Supports. *ACS Catal.* **2022**, *12*, 7233–7242.

(33) Ren, W.; Xu, A.; Chan, K.; Hu, X. A Cation Concentration Gradient Approach to Tune the Selectivity and Activity of CO₂ Electroreduction. *Angew. Chem., Int. Ed.* **2022**, *61*, No. e202214173.

(34) Warshel, A.; Sharma, P. K.; Kato, M.; Xiang, Y.; Liu, H.; Olsson, M. H. M. Electrostatic Basis for Enzyme Catalysis. *Chem. Rev.* **2006**, *106*, 3210–3235.

(35) Warshel, A. Electrostatic Origin of the Catalytic Power of Enzymes and the Role of Preorganized Active Sites. *J. Biol. Chem.* **1998**, *273*, 27035–27038.

(36) Grunwald, L.; Clémancey, M.; Klose, D.; Dubois, L.; Gambarelli, S.; Jeschke, G.; Wörle, M.; Blondin, G.; Mougél, V. A Complete Biomimetic Iron-Sulfur Cubane Redox Series. *Proc. Natl. Acad. Sci. U.S.A.* **2022**, *119*, No. e2122677119.

(37) Cordero, B.; Gómez, V.; Platero-Prats, A. E.; Revés, M.; Echeverría, J.; Cremades, E.; Barragán, F.; Alvarez, S. Covalent Radii Revisited. *Dalton Trans.* **2008**, 2832–2838.

(38) Roemelt, M.; Beckwith, M. A.; Duboc, C.; Collomb, M.-N.; Neese, F.; DeBeer, S. Manganese K-Edge X-Ray Absorption Spectroscopy as a Probe of the Metal–Ligand Interactions in Coordination Compounds. *Inorg. Chem.* **2012**, *51*, 680–687.

(39) Bauer, M.; Gastl, C. X-Ray Absorption in Homogeneous Catalysis Research: The Iron-Catalyzed Michael Addition Reaction by XAS, RIXS and Multi-Dimensional Spectroscopy. *Phys. Chem. Chem. Phys.* **2010**, *12*, 5575.

(40) Kau, L. S.; Spira-Solomon, D. J.; Penner-Hahn, J. E.; Hodgson, K. O.; Solomon, E. I. X-Ray Absorption Edge Determination of the Oxidation State and Coordination Number of Copper. Application to the Type 3 Site in Rhus Vernicifera Laccase and Its Reaction with Oxygen. *J. Am. Chem. Soc.* **1987**, *109*, 6433–6442.

(41) Walroth, R. C.; Uebler, J. W. H.; Lancaster, K. M. Probing Cu^I in Homogeneous Catalysis Using High-Energy-Resolution Fluorescence-Detected X-Ray Absorption Spectroscopy. *Chem. Commun.* **2015**, *51*, 9864–9867.

(42) Solomon, E. I. Spectroscopic Methods in Bioinorganic Chemistry: Blue to Green to Red Copper Sites. *Inorg. Chem.* **2006**, *45*, 8012–8025.

(43) Rudolph, J.; Jacob, C. R. Revisiting the Dependence of Cu K-Edge X-Ray Absorption Spectra on Oxidation State and Coordination Environment. *Inorg. Chem.* **2018**, *57*, 10591–10607.

(44) Bats, J. W.; Kretz, T.; Lerner, H.-W. A Polymorph of Tetra-kis(Acetonitrile-KN)Copper(I) Tetra-fluoridoborate. *Acta Crystallogr., Sect. C: Cryst. Struct. Commun.* **2009**, *65*, m94–m96.

(45) Kleinwächter, M.; Vendier, L.; Dinoi, C.; Etienne, M. Tuning Stoichiometry and Supramolecular Assembly in Perfluorinated Indazolato Coinage Metal Complexes. *Dalton Trans.* **2013**, *42*, 10102–10105.

(46) Foltling, K.; Huffman, J.; Mahoney, W. Structure of Chlorotris-(Triphenylphosphine)Copper(I)–Tetrahydrofuran (1/3). *Acta Crystallogr., Sect. C: Cryst. Struct. Commun.* **1987**, *C43*, 1490–1492.

(47) Carlson, T. F.; Fackler, J. P., Jr.; Kresinski, R. A. Chlorotris-(Triphenylphosphine)Copper(I) Tetrahydrofuran Solvate. *Acta Crystallogr., Sect. C: Cryst. Struct. Commun.* **1996**, *52*, 1117–1119.

(48) Kräuter, T.; Neumüller, B. Triphenylphosphane Complexes of Copper(I): Structural and ^{31}P NMR Investigations. *Polyhedron* **1996**, *15*, 2851–2857.

(49) Bowmaker, G. A.; Dyason, J. C.; Healy, P. C.; Engelhardt, L. M.; Pakawatchai, C.; White, A. H. Lewis-Base Adducts of Group 11 Metal(I) Compounds. Part 27. Solid-State Phosphorus- 31 Cross-Polarization Magic-Angle Spinning Nuclear Magnetic Resonance, Far-Infrared, and Structural Studies on the Mononuclear 2:1 Adducts of Triphenylphosphine with Copper(I) and Gold(I) Halides. *J. Chem. Soc., Dalton Trans.* **1987**, 1089–1097.

(50) Brown, I. D.; Dunitz, J. D. The Crystal Structure of Diazoaminobenzene Copper(I). *Acta Crystallogr.* **1961**, *14*, 480–485.

(51) Darensbourg, D. J.; Holtcamp, M. W.; Klausmeyer, K. K.; Reibenspies, J. H. Crystal Structure of Di- μ -Chloro-Tris-(Triphenylphosphine)Dicopper(I)-Dichloromethane, $\text{C}_{55}\text{H}_{47}\text{Cl}_4\text{Cu}_2\text{P}_3$. *Z. Für Krist. - Cryst. Mater.* **1995**, *210*, 615–616.

(52) Wei, M.; Willett, R. D. A Comparison of the Crystal Structures of $(\text{DabcoH}_2)\text{CuCl}_4$ and $(\text{DabcoH}_2)\text{CuCl}_4\cdot\text{H}_2\text{O}$. *J. Chem. Crystallogr.* **2002**, *32*, 439–445.

(53) Willett, R. D.; Jardine, F. H.; Rouse, I.; Wong, R. J.; Landee, C. P.; Numata, M. Crystal Structure, Magnetic Susceptibility, and EPR Study of Bis-(β -Alaninium) Tetrachlorocuprate(II): Spin-Diffusion Effects in a Two-Dimensional Square Planar Ferromagnet with Anisotropic and Antisymmetric Exchange. *Phys. Rev. B* **1981**, *24*, 5372–5381.

(54) Walroth, R. C.; Lukens, J. T.; MacMillan, S. N.; Finkelstein, K. D.; Lancaster, K. M. Spectroscopic Evidence for a $3d^{10}$ Ground State Electronic Configuration and Ligand Field Inversion in $[\text{Cu}(\text{CF}_3)_4]^{1-}$. *J. Am. Chem. Soc.* **2016**, *138*, 1922–1931.

(55) DiMucci, I. M.; Lukens, J. T.; Chatterjee, S.; Carsch, K. M.; Titus, C. J.; Lee, S. J.; Nordlund, D.; Betley, T. A.; MacMillan, S. N.; Lancaster, K. M. The Myth of d^8 Copper(III). *J. Am. Chem. Soc.* **2019**, *141*, 18508–18520.

(56) Shoshani, M. M.; Agapie, T. Ligand Architecture for Triangular Metal Complexes: A High Oxidation State Ni_3 Cluster with Proximal Metal Arrangement. *Chem. Commun.* **2020**, *56*, 11279–11282.

(57) Santra, A.; Gupta, G.; Biswas, B.; Das, A.; Ghosh, D.; Paria, S. Understanding the Effect of Internal Electrostatic Fields Created by Alkaline Earth Metal Ions Poised over Secondary Coordination Sphere of Molecular Iron Complexes. *Inorg. Chem.* **2023**, *62*, 9818–9826.